Geophysical Research letters

Supporting Information for

# An 8-month slow slip event triggers progressive nucleation of the 2014 Chile megathrust

Anne Socquet[1], Jesus Piña Valdes[1], Jorge Jara[1], Fabrice Cotton[2,3], Andrea Walpersdorf[1], Nathalie Cotte[1], Sebastian Specht[2,3], Francisco Ortega-Culaciati[4,5], Daniel Carrizo[5], Edmundo Norabuena[6]

[1] Univ. Grenoble Alpes, Univ. Savoie Mont Blanc, CNRS, IRD, IFSTTAR, ISTerre, F-38000 Grenoble

[2] GFZ Helmholtz Centre Potsdam, German Research Centre for Geosciences, Telegrafenberg, 14473 Potsdam, Germany.

[3] Potsdam University, Potsdam, Germany

[4] Department of Geophysics, Faculty of Physical and Mathematical Sciences, University of Chile, Santiago, Chile.

[5] Advanced Mining Technology Center, Faculty of Physical and Mathematical Sciences, Universidad de Chile, Santiago, Chile.

[6] Instituto Geofisico del Peru, Lima, Peru

Cite as: Socquet, A., Piña Valdes, J. P., Jara, J., Cotton, F., Walpersdorf, A., Cotte, N., Specht, S., Ortega-Culaciati, F., Carrizo, D., and Norabuena, E. (2017), *An 8 month slow slip event triggers progressive nucleation of the 2014 Chile megathrust*, **Geophysical Research Letters**, 44 doi:10.1002/2017GL073023.

## Contents of this file



## Introduction

This supporting information provides a general description of the methods and processing steps used and supplementary figures that support our findings.

## **Text S1: Methods**

cGPS data analysis

Daily cGPS processing

We used data from several cGPS networks spanning the whole central Andes subduction (IPOC, LIA Montessus de Ballore, ISTerre, and Caltech Andean Observatory), together with IGS stations. These cGPS data were analyzed in double differences, in two distinct regional subnetworks, plus a global network **(Figure S1)**. The fifty stations available during the period 2000–2014 were used to design the first regional subnetwork. The second regional subnetwork includes 50 stations running from 2007 to 2014, 33 stations overlapping with the first subnetwork in order to ensure consistency between the subnetworks. The global network includes 99 IGS sites worldwide, 22 of them in South America, with 49 stations overlapping with the two regional subnetworks. 24-hour sessions were reduced to daily estimates of station positions using the GAMIT 10.5 software, choosing the ionosphere-free combination, and fixing the ambiguities to integer values. We use precise orbits from the International GNSS Service for Geodynamics, precise EOPs from the IERS bulletin B, IGS tables to describe the phase centers of the antennas, FES2004 ocean-tidal loading corrections, as well as atmospheric loading corrections (tidal and non-tidal). We estimated one tropospheric zenith delay parameter every two hours and one couple of horizontal tropospheric gradients per 24h session, using the Vienna Mapping Function (VMF1) [Boehm et al., 2006], to map the tropospheric delay in zenithal direction, with a priori ZHD evaluated from pressure and temperature values from the VMF1 grids. Daily solutions are combined using the GLOBK software in a "regional stabilization" approach, and mapped it into the ITRF2008 reference frame [Altamimi et al., 2011] by adjusting selected stations coordinates to those defined in the ITRF in a least square iterative process.

Time series analysis and identification of transient movements

Annual and semi-annual signals were removed from the obtained daily time series, as well as the long-term constant deformation associated with interseismic loading, by fitting a linear regression together with a pair of sinusoids terms. The remaining noise has been reduced by removing the common-mode, obtained by selecting stations located within a distance range of 50-500km from the source region (SJUA, ATIC, CHRA, PTCL, LYAR, UTAR, PCCL, PB02, PB04, MLCA, PB05, PMEJ, JRGN, UCNF, NZCA, AREQ, TORA, TQPL, DANC, TRTA, PALC, PTRE, MNMI, COLC, CHMZ, PB11, PCHA, PB08, PB01, PB07, PB03, CDLC, RADO, PB06, CBAA, VLZL, CJNT) and by averaging their detrended signals. Then, in order to mitigate the residual loading signal present in our signal, we removed from each time series the mean annual residual seasonal movement computed between 2010 and 2013. This procedure reduced significantly the scatter in our time series. In order to study the long term transient in our time series, we excluded data after March 15$^{th}$, 2014 (when a strong preseismic signal occurred), and then computed the average velocity variations, by fitting a linear regression in a six-month sliding window of the obtained detrended and de-noised time-series. The results indicate a velocity change in July 2013 (appr. eight months before the mainshock) at coastal stations located at 20.3°S close to the city of Iquique. This velocity change propagated bilaterally and reached stations located within a distance of appr. 100km parallel to the strike of the subduction (parallel to the coastline). In a second step, we compute the average velocities by fitting a linear regression to the detrended cGPS time series on three different time periods before July 2013 (interseismic), July 2013- 13$^{th}$ March 2014 (preseismic 1), 14$^{th}$ March 2014-March 31$^{st}$ 2014 (preseismic 2) **(Figures S2 and S3)**. Uncertainties on linear regressions correspond to standard deviation of one for each linear regression. Displacements for both pre-seismic periods have been obtained by multiplying each station velocity by the time span. For the preseismic period 1, we selected only stations showing a continuous time series since 2012, to avoid artifacts associated with jumps or data holes in the time series. For both preseismic periods, we discarded noisy time series generating the largest uncertainties in the displacement computation.

<u>Slip distribution inversion and resolution</u>

The surface deformation fields associated with the coseismic and preseismic phases were modeled using a dislocation buried in a layered elastic half space [Wang et al., 2003], taking crust1.0 as a velocity model. The fault geometry was constrained by the trace of the trench at the surface. We assumed a uniform dip of 15° and a variable rake, so that the slip direction is parallel to the plate convergence (76°), and is taken constant at all patches.

The fault was discretized into an array of 24 × 11 elements, measuring approximately 15x15km, although their size varies locally since the fault follows the trench geometry **(Figures S4, S5 & S6)**. To solve for the slip distribution along the 264 fault patches, we used a least squares minimization with a non-negativity constraint on the slip. Slip was forced to zero at the edges of the fault. To limit oscillations of the solution, we applied smoothing by minimizing the second-order derivative of the fault slip. We determined the optimal solution roughness [Jonsson et al., 2002] that was used in our final models searching for a compromise between the roughness and misfit of the solution. We estimate the sensitivity of our data set to unit displacements on each node of the grid by summing the horizontal deformation on the whole network after Loveless et al. [2011]. The power of our data to constrain the coupling on the interface is high from 15 km depth to more than 70 km depth in general.

The coseismic offsets extracted from cGPS time series were used to invert for the coseismic slip **(Figure S4)**. The roughness of the preferred co-seismic distribution is 0.04 cm/km for a RMS (L2-norm misfit) of 1.20 cm. The seismic moment is 1.7 $10^{21}$N.m, and corresponds to a Magnitude 8.1. The inverted slip distribution for pre-seismic period 2 **(Figure S5)** corresponds to a moment Mo=3.9 $10^{19}$N.m (Mw=7.0) and a fit to the data with RMS= 1.3mm. The inverted slip distribution for pre-seismic period 1 **(Figure S6)** corresponds to a moment Mo=7 $10^{18}$N.m (Mw=6.5) and a fit to the data with RMS= 0.5mm **(Figure S7)**. Because we were able to estimate accurately the long term transient displacement on a subset of stations only, mostly located along the coast, the slip distribution for pre-seismic period 1 less well constrained than the co-seismic and pre-seismic period 2. However, the patches that are found to be slipping by our inversions are located in zones that are well constrained by our data **(Figure S6)**. Depending on the smoothing applied to the model, the estimate of the geodetic moment of pre-seismic slow slip events (for periods 1 and 2) vary within less than 10% **(Figure S7**), and the main features of the slip distribution are quite stable whatever the smoothing applied **(Figure S8)**.

Interface Seismic Catalog

The interface seismicity catalog **(Figure S9)** was compiled from the GEOFON moment tensor catalog (http://geofon.gfz-potsdam.de/eqinfo/list.php?mode=mt) and the Global CMT catalog (http://www.globalcmt.org/CMTsearch.html). We use ACE, a data driven algorithm to automatically determine focal mechanism clusters with similar Style-of-Faulting (strike, rake, and dip). The algorithm is also capable to identify the nodal planes as rupture and auxiliary planes, therefore allowing the computation of the rupture plane distance. Since the rupture plane size is unknown, we used a rupture plane scaling relation [Strasser et al., 2009]. Hypocenters are not directly required to classify the data and therefore, classification errors are reduced, compared to classical deterministic classification scheme. We checked that this data-driven procedure was giving results consistent with a more classical classification and that the locations of the earthquakes identified as interface earthquakes were consistent with the known subduction fault plane geometry. This procedure allowed us to build a catalogue containing 125 interface earthquakes in North Chile between January 2008 and June 2014, from 19°S to 21°S and 72°W to 67°W, shallower than 80 km, with Mw equal or higher than 4.5 **(Figures S9 and S10)**. Location and depth of earthquakes can be poorly constrained in the area (see the dispersion in the seismicity and the discrepancy with the trace of the slab in **Figure S10**), demonstrating that the strategy of using the focal mechanisms to identify interface events is better adapted than a strategy based on earthquakes depth or location.

Validation of the Ground Motion Prediction Equations (GMPEs) for the studied seismic crisis

The prediction of ground motion was done using the Abrahamson et al. [2015] Prediction Model. GMPEs predict the Acceleration Response spectra, which correspond to the maximum acceleration experimented by an oscillator of a given mass with one degree of freedom (at different fundamental periods) for different input parameters (e.g. distance to the source, site conditions, magnitude). Abrahamson et al. [2015] model is recognized as one of the leading models to predict ground-motions in subduction areas and has been recently selected for the Global Earthquake Model [Stewart et al., 2015]. To apply this model, Vs30 = 850 m/s was assumed for all stations of the network based on the information that the stations are located on bedrock. The distance between each site and the rupture plane has been estimated directly from the hypocentral distances [Händel et al., 2014].

The fit of the model was tested for oscillators frequencies of 0.75 Hz, 1 Hz, 1.25 Hz, 5 Hz, 10 Hz and for PGA. Residuals have been computed and normalized by the standard deviation of the GMPE model. Therefore a residual value of one means that the observation is offset from the mean predicted value by one model standard deviation. The distribution of absolute residuals allows to evaluate how good is the predictive model in terms of consistency (i.e. do the residuals follow a similar probabilistic distribution than the random error of the model with respect to dataset used to calibrate the model?), precession and accuracy (i.e. are the observed normalized residuals centered on zero?). The obtained absolute residual distribution shows both a good residual distribution and a reasonable fit of the model, with a somewhat lower accuracy between 0.75 Hz and 5 Hz (**Figure S12**).

GMPEs residuals can be separated in two residuals terms: between-event and within-event residuals [Abrahamson and Youngs 1992]. The within-event residuals correspond to the difference between each observation and the median of the observations. Its distribution provides an estimation of the variability of record specific factor as site amplification (i.e. variability in site conditions effects) [Strasser et al. 2010, Al Atik et al, 2010]. The within-event residual distribution shows also a good fit, indicating that site effects variability is well estimated by the model (**Figure S13**).

The between-event residuals represent the difference between the median of the observations of a given event, with respect to the median of the model [Abrahamson and Youngs, 1992]. The between-event residual distribution (**Figure S14**) can be interpreted as the variability of wave radiation due to source parameters (e.g. stress-drop) that are not included in the prediction model [Atik et al., 2010; Youngs et al., 1995]. Tests performed with other recent subductions GMPE's did not show a better global agreement and therefore the Abrahamson et al. [2015] model was chosen as the backbone model to predict ground-motions for the North Chile subduction area.

**References:**

Abrahamson N., Gregor N., K. Addo, BC Hydro Ground Motion Prediction Equations For Subduction Earthquakes. Earthquake Spectra, (2015) doi: http://dx.doi.org/10.1193/051712EQS188MR.

Abrahamson, N. A., and R. R. Youngs (1992). A stable algorithm for regression analyses using the random effects model, Bulletin of the Seismological Society of America **82** 505-510.

Z. Altamimi, X. Collilieux, L. Métivier, ITRF2008: An improved solution of the international terrestrial reference frame. J. Geod. 85, 457–473 (2011). doi:10.1007/s00190-011-0444-4

Atik L. A., Abrahamson N., Bommer J. J., Scherbaum F., Cotton F., Kuehn N. (2010). The Variability of Ground-Motion Prediction Models and Its Components. Seismological Research Letters, 81(5), 794-801. doi:10.1785/gssrl.81.5.794

Bindi, D., S. Parolai, E. Görgün, H. Grosser, C. Milkereit, M. Bohnhoff, E. Durukal (2007). ML scale in Northwestern Turkey from 1999 Izmit aftershocks: updates., Bull. Seism. Soc. of Am., Vol. 97, No. 1B, pp. 331–338, doi: 10.1785/0120060071

Boehm J, Werl B, Schuh H, Troposphere mapping functions for GPS and very long baseline interferometry from European Centre for Medium-Range Weather Forecasts operational analysis data, J Geophys Res 111:B02406. doi:10.1029/2005JB003629, (2006).

Boore D. M., Sisi A. A., Akkar S., Using Pad Stripped Acausally Filtered Strong Motion Data. Bulletin of the Seismological Society of America, 102(2), 751-760 (2012).

Chiou B., Darragh R., Gregor, N., Silva W., NGA project strong-motion database. Earthquake Spectra, 24(1), 23-44 (2008).

Händel A., Specht S., Kühn N. M., Scherbaum, F. (2014). Mixtures of ground-motion prediction equations as backbone models for a logic tree: an application to the subduction zone in Northern Chile. Bulletin of Earthquake Engineering, 13(2), 483-501. doi:10.1007/s10518-014-9636-7.

Jonsson, S., H. Zebker, P. Segall, and F. Amelung, Fault Slip Distribution of the 1999 Mw 7.1 Hector Mine, California, Earthquake, Estimated from Satellite Radar and GPS Measurements, Bull. Seismol. Soc. Am., 92(4), 1377–1389, (2002). doi: 10.1785/0120000922.

Loveless, J. P., and B. J. Meade (2011), Spatial correlation of interseismic coupling and coseismic rupture extent of the 2011 MW = 9.0 Tohoku Oki earthquake, Geophys. Res. Lett., 38, L17306, doi:10.1029/2011GL048561.

Nigam N. C., Jennings P. C. (1969). Calculation of response spectra from strong-motion earthquake records. Bulletin of the Seismological Society of America, 59(2), 909-922.

Stewart J. P., Douglas J., Javanbarg M., Bozorgnia Y., Abrahamson N. A., Boore D. M., Campbell K. W., Delavaud E., Erdik M., Stafford P. J. (2015) Selection of Ground Motion Prediction Equations for the Global Earthquake Model. Earthquake Spectra, 31, 1, 19-45, doi: http://dx.doi.org/10.1193/013013EQS017M.

Strasser F. O., Abrahamson N. A., Bommer J. J., Sigma: Issues, Insights, and Challenges. Seismological Research Letters, 80(1), (2009) 40-56. doi:10.1785/gssrl.80.1.40

Strasser, F. O., M. C. Arango, and J. J. Bommer (2010). Scaling of the Source Dimensions of Interface and Intraslab Subduction-zone Earthquakes with Moment Magnitude, Seismological Research Letters 81 941-950.

Wang R., F. Lorenzo-Martín, F. Roth, Computation of deformation induced by earthquakes in a multi-layered elastic crust - FORTRAN programs EDGRN/EDCMP, Computer and Geosciences, 29(2), 195-207 (2003).

Youngs R. R., Abrahamson N., Makdisi F. I., Sadigh K. (1995). Magnitude-dependent variance of peak ground acceleration. Bulletin of the Seismological Society of America, 85(4), 1161-1176.

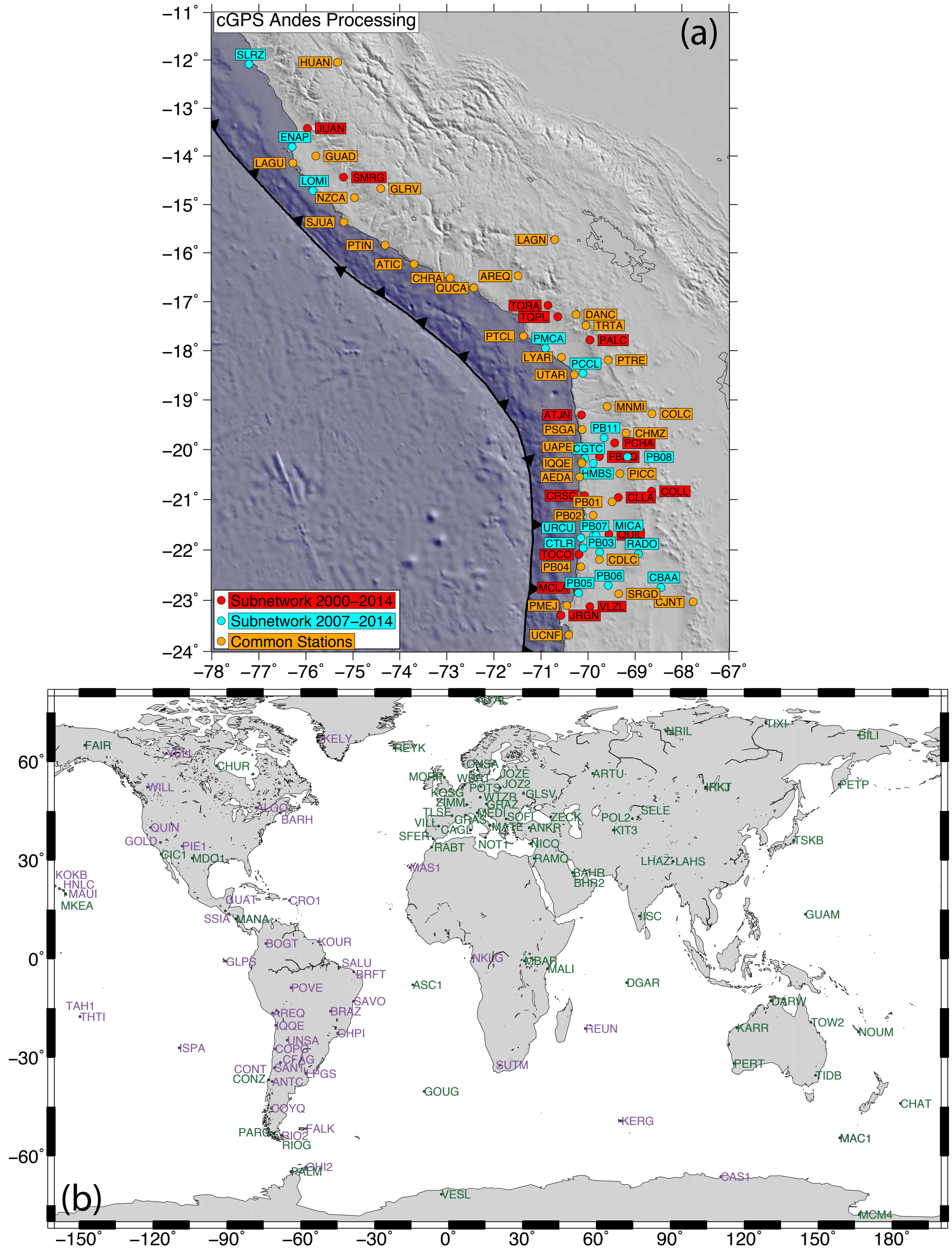


**Figure S1** : Map of the network used in this study, showing the three subnetworks (Andes 2000 – 2014, Andes 2007 – 2014 (a) , and the Global Network (b)), as well as the stations used for the reference frame computation. Green color in (b) indicates IGS stations included for global processing, while purple indicates IGS stations overlapping with the Andes subtnetworks.

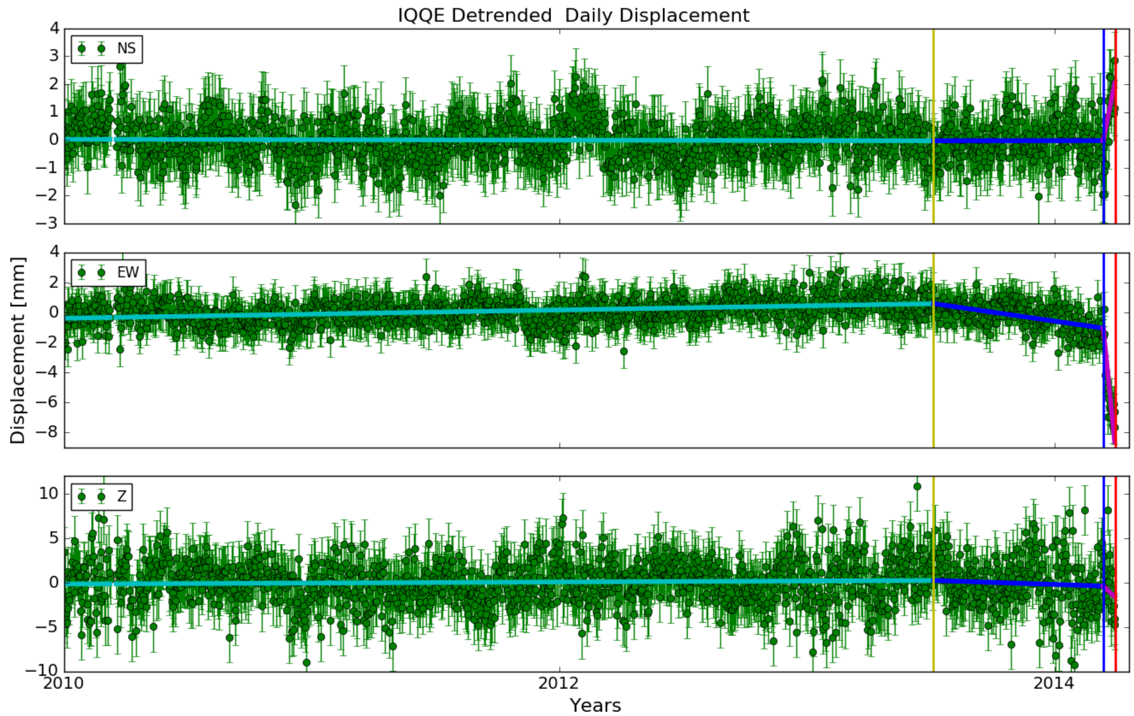


**Figure S2** : N, E, U detrended daily displacements for IQQE station since 2010. Vertical lines indicate the dates of the swarm of July 2013 (yellow), the Mw6.7 foreshock on March 16th 2014 (blue) and the Mw 8.1 main shock on April 1st 2014 (red). Linear regressions for the three preseismic periods are shown.

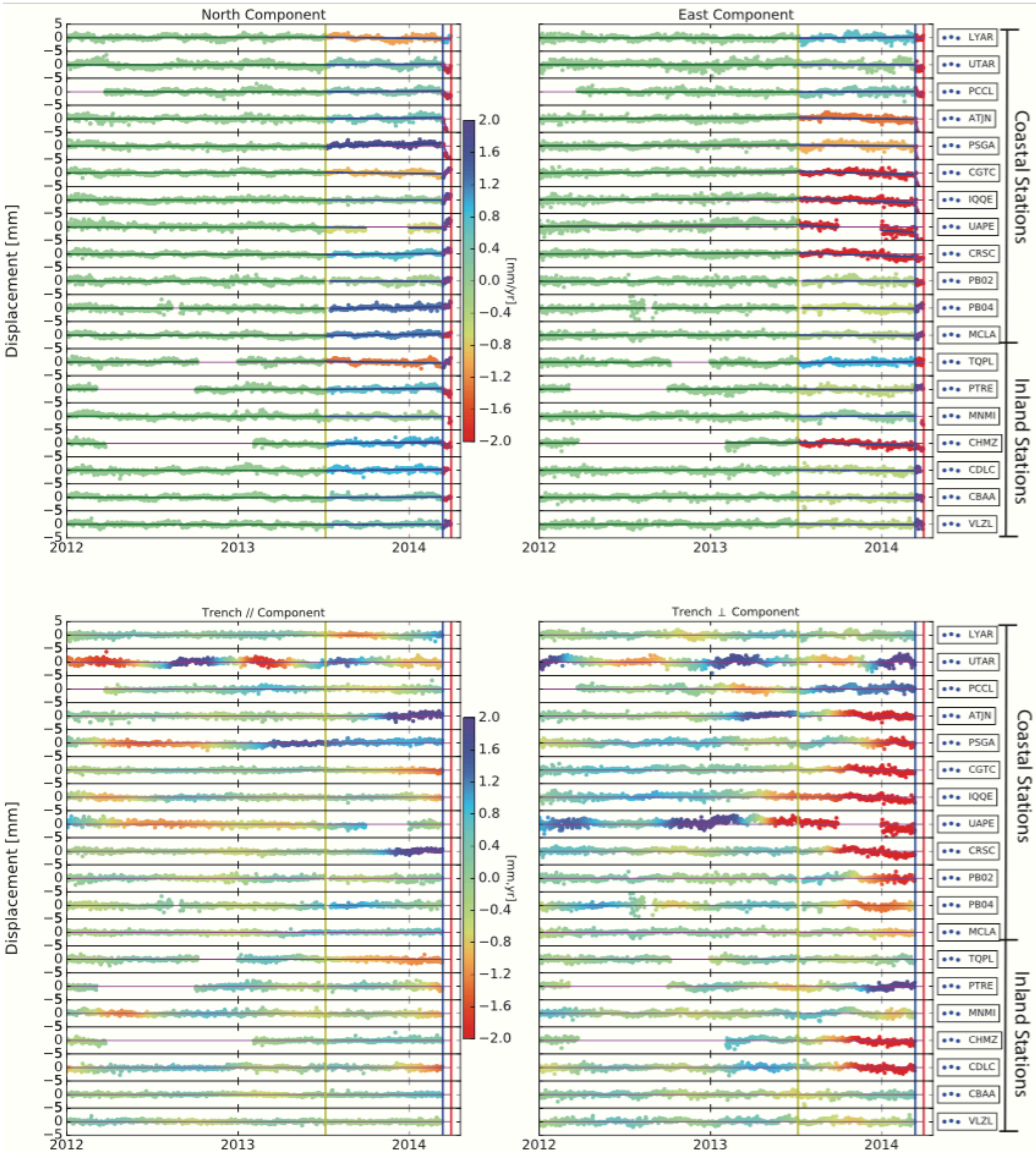


**Figure S3** : Detrended displacement time series for a selection of stations along the coast and inland. Bottom 2 panels: Colors, indicate the trench parallel (left panels) and trench perpendicular (right panels) velocities obtained by computing the average velocity over a six-month sliding window. Top 2 panels: Colors, indicate the N-S (left panels) and E-W (right panels) velocities obtained by fitting a linear regression on the displacement time series for the three preseismic periods.

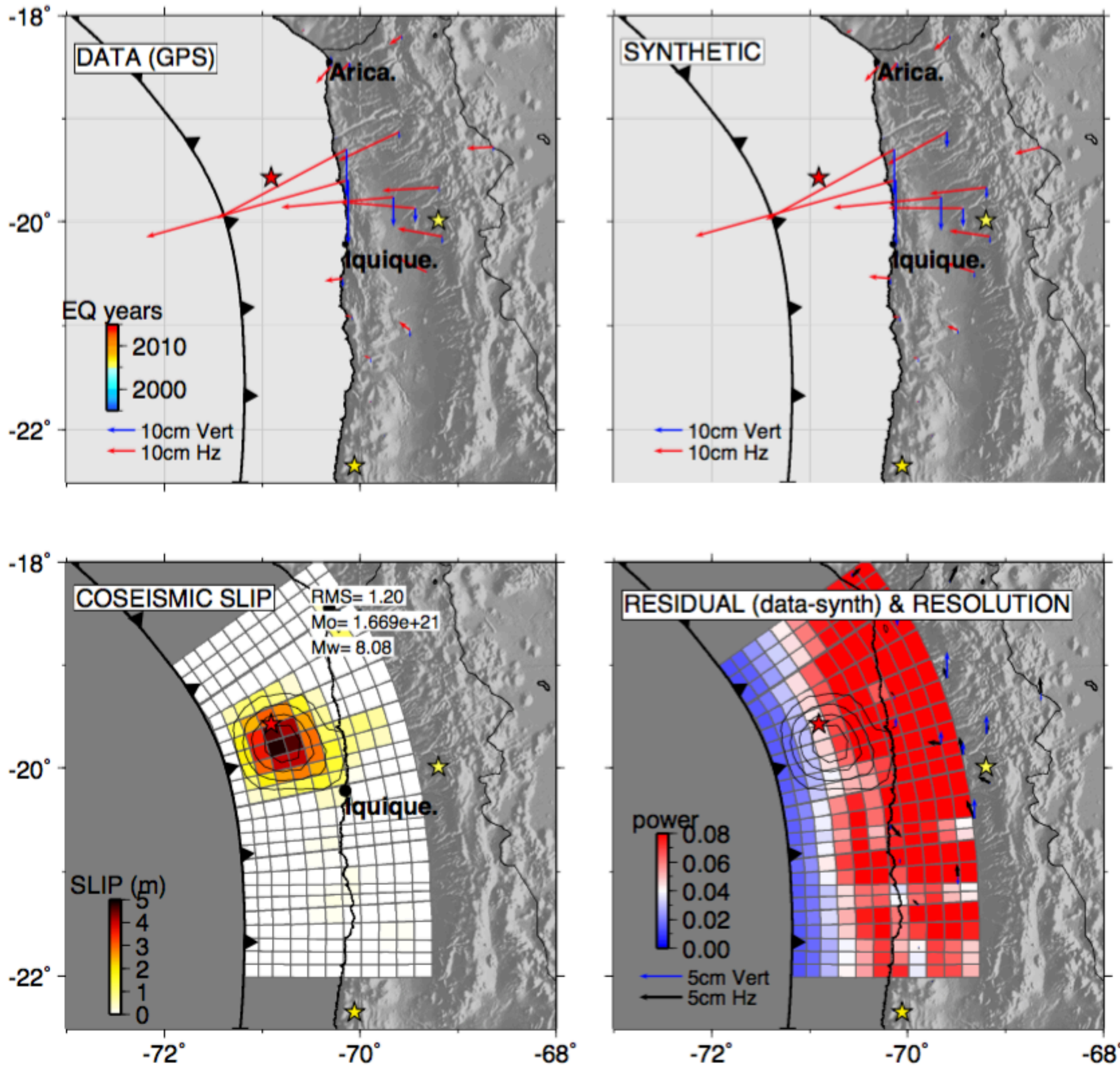


**Figure S4** : Co-seismic displacements (observed : top left, and modeled: top right), co-seismic slip distribution inverted from surface displacements (bottom left), residuals and power of GPS stations to constrain plate interface behavior (i.e., sum of the partial derivatives relating GPS displacement to unit slip [Loveless & Meade, 2011]) (bottom right). One-meter contours are drawn.

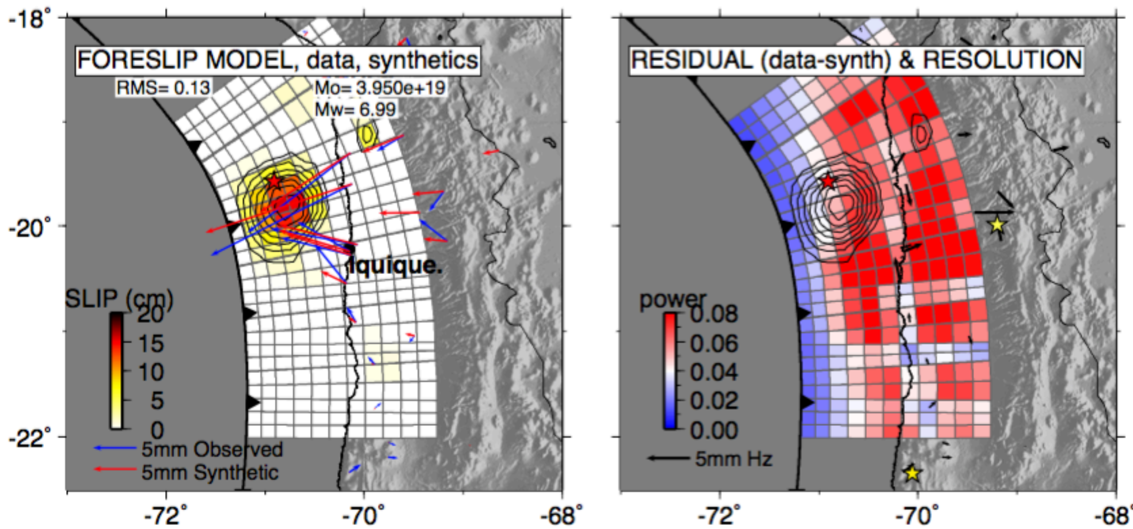


**Figure S5** : Left: Displacements (observed: blue, modeled: red) during preseismic period 2 (March 14$^{th}$ 2014 to March 31$^{st}$ 2014) and preseismic slip distribution for the two weeks preceding the main shock inverted from surface displacements, Right: residuals and resolution. Two-cm contours are drawn.

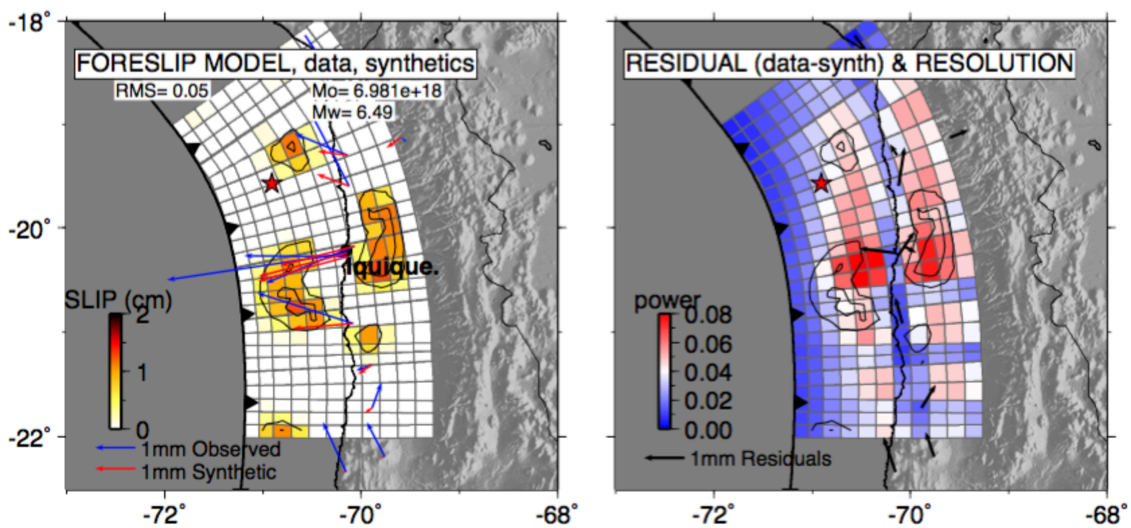


**Figure S6** : Left: Displacements (observed: blue, modeled: red) during preseismic period 1 (July 6$^{th}$ 2013 to March 13$^{th}$ 2014) and preseismic slip distribution for the two weeks preceding the main shock inverted from surface displacements, Right: residuals and resolution. Five-mm contours are drawn.

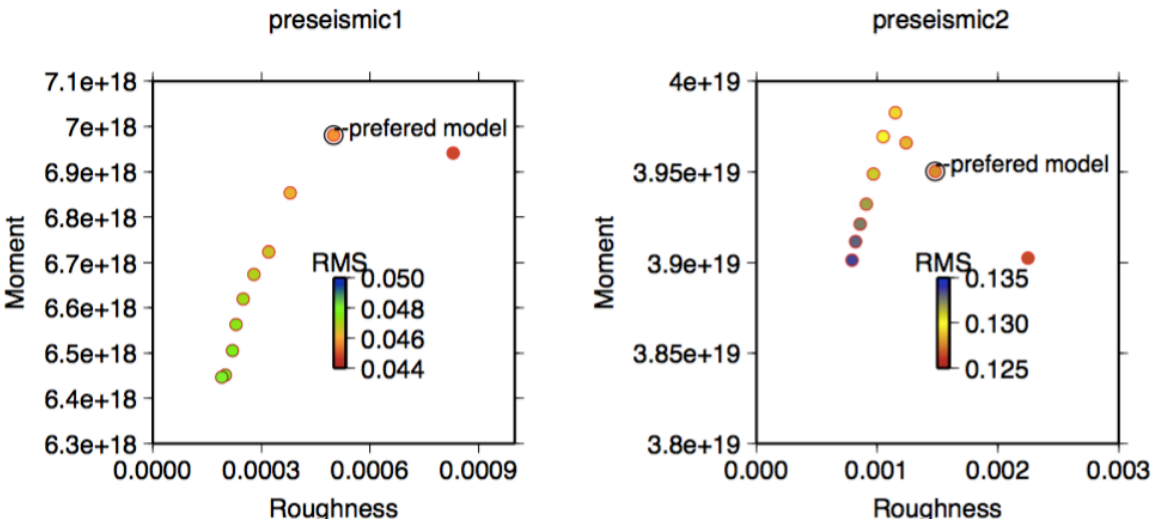


**Figure S7:** Geodetic moment as a function of the model roughness, for both preseismic models. Dots are color coded with the model – data misfit. The preferred model is chosen as a compromise between smoothness and RMS.

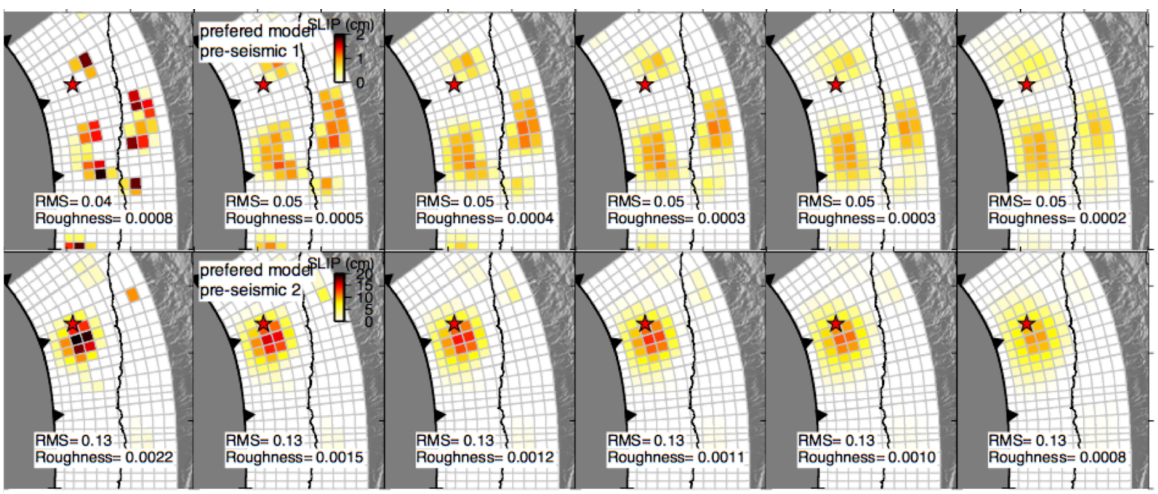


Figure S8: Pre-seismic slip distribution for different model roughnesses. Top: 8 months preseismic (july 2013 – mid-March 2014), Bottom: 15-day pre-seismic (Mid-March to End March 2014).

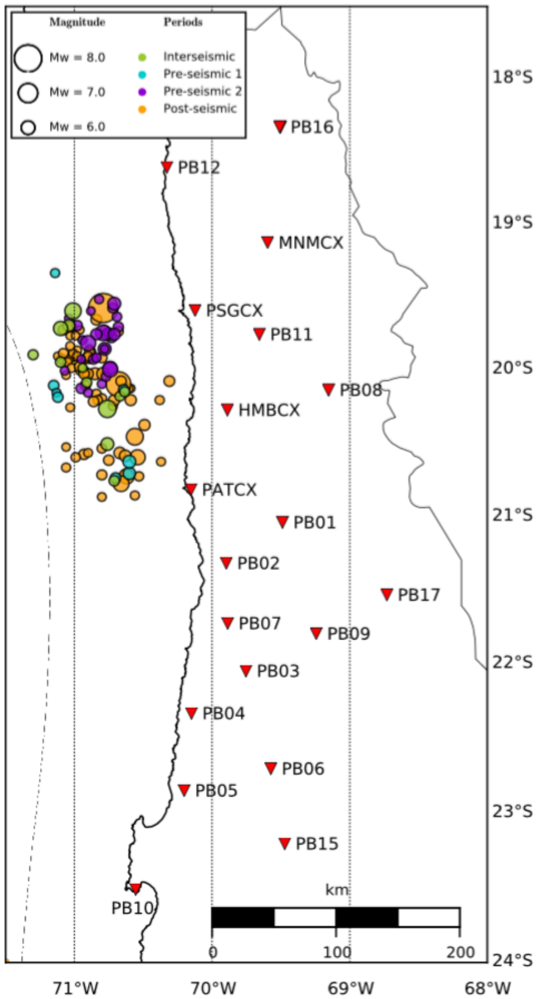


**Figure S9:** Map of the interface seismicity data set (dots colored as a function of the 4 periods defined in the paper), and network of IPOC accelerometric stations (red inverted triangles) used to perform earthquakes frequency content analysis. All these stations are installed on bedrock. Most of them are also colocated with GPS stations used in this paper.

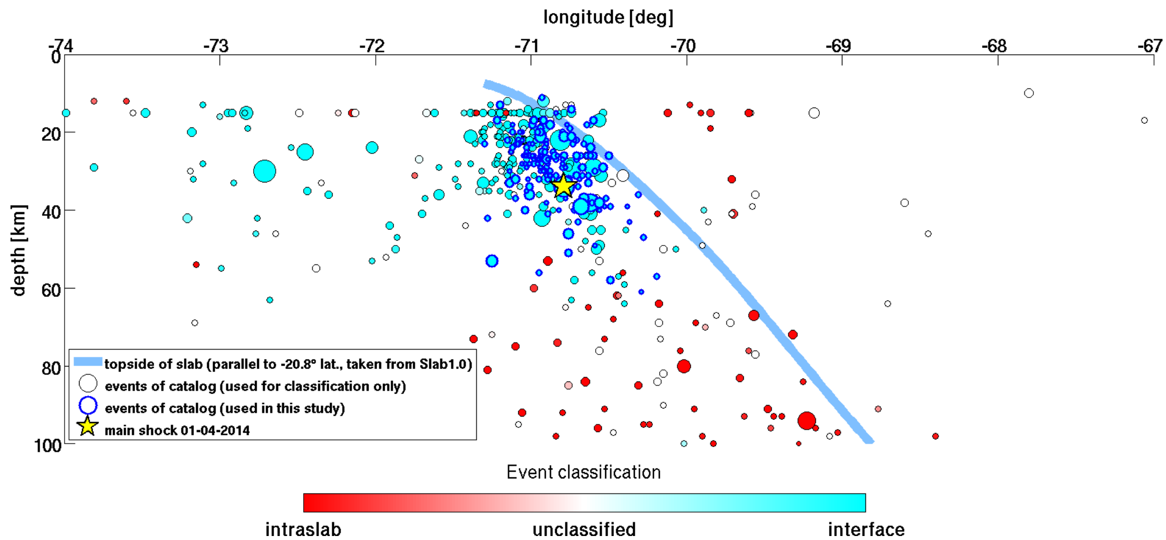


**Figure S10:** Cross section of IPOC catalogue of earthquakes in North Chile. Colored dots represents the classification of earthquakes (interface, unclassified or intraplate) as a function of their focal mechanism. The blue line represents the Slab1.0 subduction interface. The events used in this study (contoured in blue) have been selected as being interface events that occurred between January 2008 and June 2014.

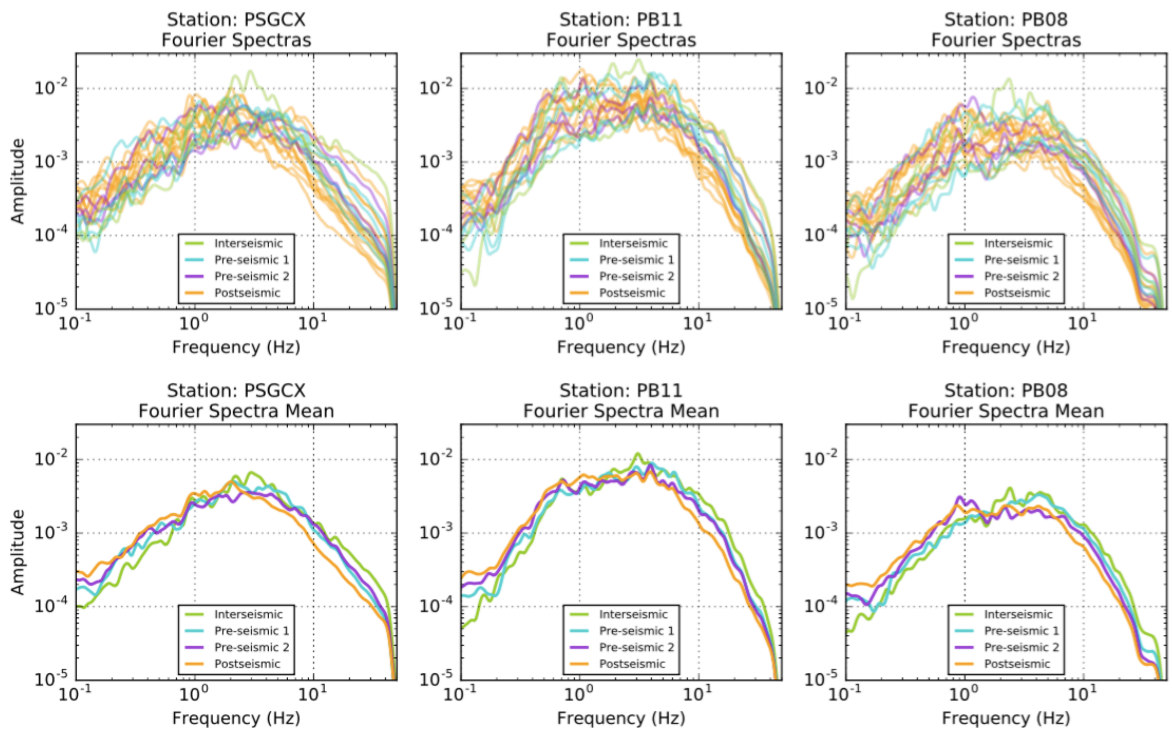


**Figure S11:** Acceleration Fourier Spectra computed at stations PSGX, PB11 and PB08 (see **Figure S9** for location) for interface earthquake within 5.1-5.2 Magnitude range. Spectra are color-coded as function of the period when occured the earthquake (interseismic in green, pre-seismic 1 in cyan, pre-seismic 2 in purple, post-seismic in orange). Top line shows all individual spectra while bottom line shows the mean spectrum for each time period.

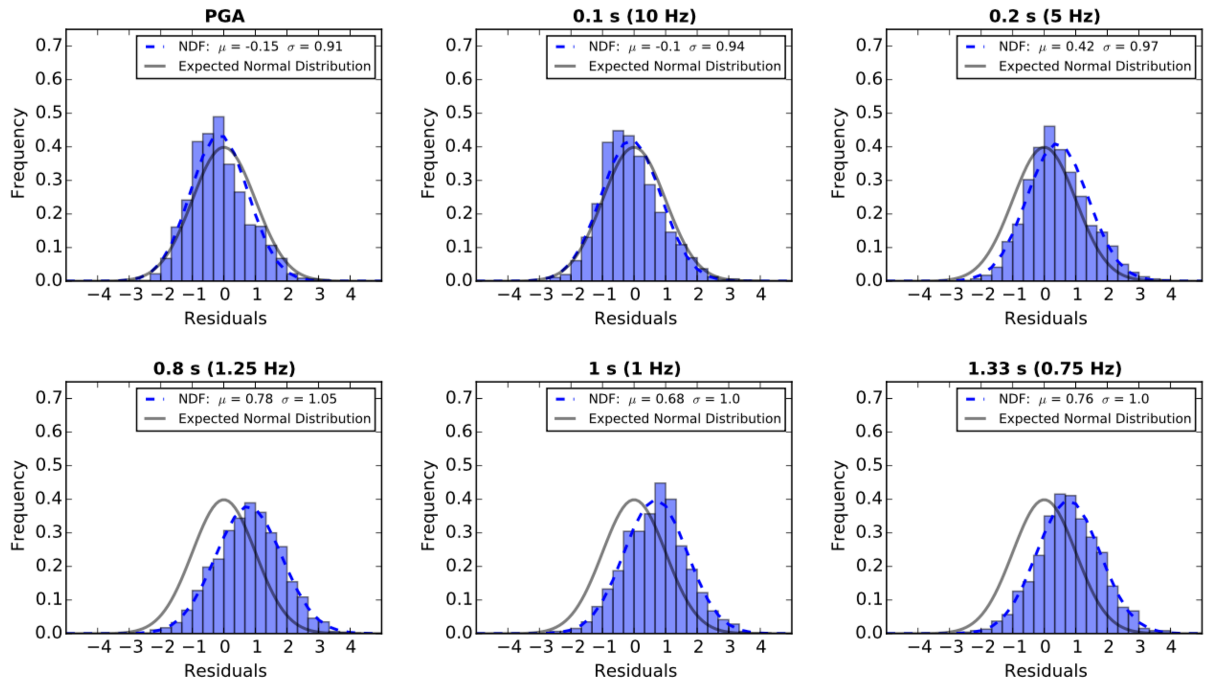


**Figure S12:** Histograms of ground motion absolute residuals normalized with respect to the total standard deviation of the GMPE model [Abrahamson et al., 2015]. The Normal Density Function (NDF) of the residuals is shown by the dashed lines and the expected normal distribution is represented by the gray lines.

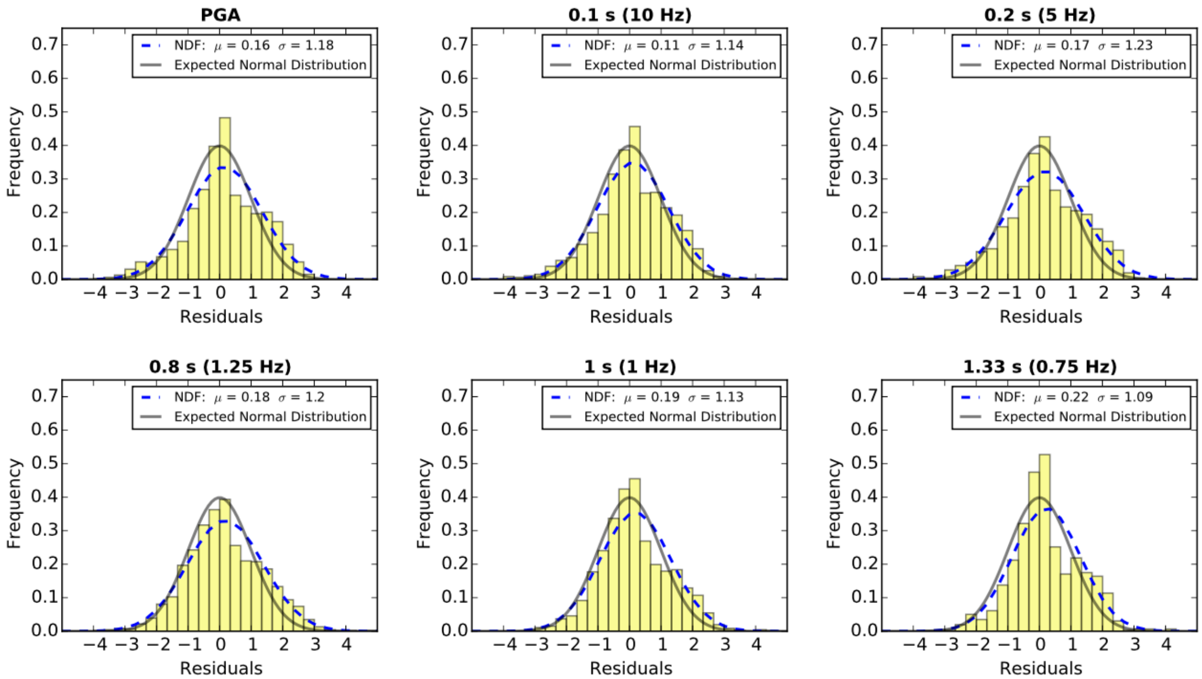


**Figure S13:** Histograms of the Within-Events residuals normalized with respect to the Within-Event standard deviation of the model. The Normal Density Function (NDF) of the residuals is shown by dashed lines and the expected normal distribution by gray lines.

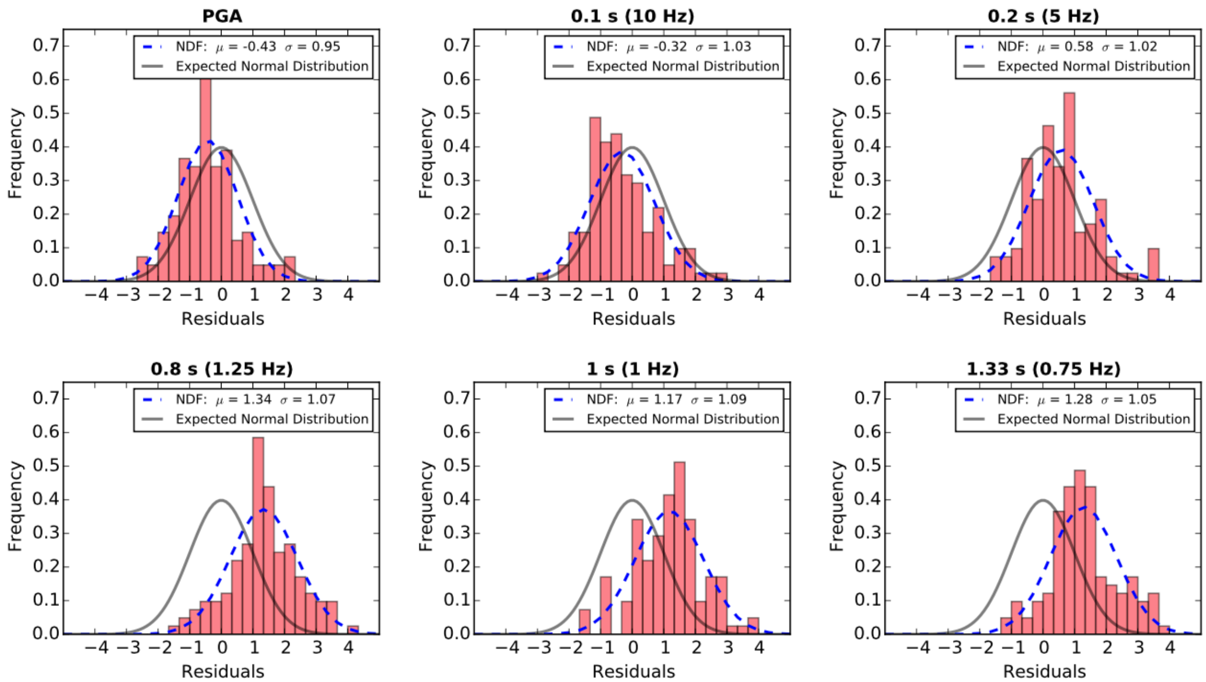


**Figure S14:** Histograms of the Between-Event residuals normalized with respect to the Between-Event standard deviation of the model. The Normal Density Function (NDF) of the residuals is shown by dashed lines and the expected normal distribution by gray lines.

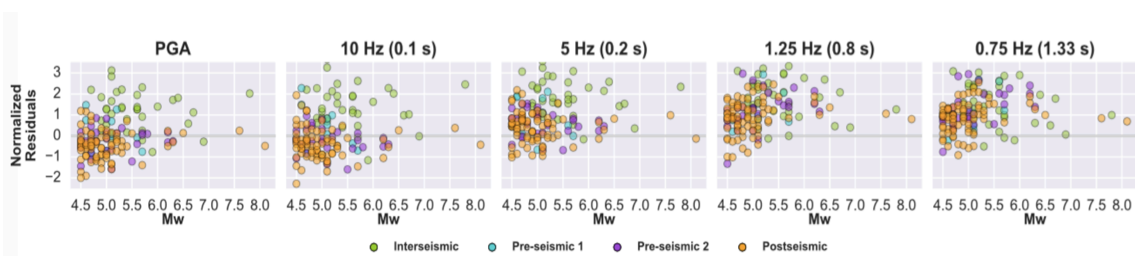


**Figure S15:** Between-event residuals as a function of event magnitude at the different frequency values shown in figure 1 (mid-panel). At frequencies above 5Hz, earthquakes occurring during the interseismic period exhibit significantly larger residuals than earthquakes belonging to preseismic and postseismic sequences. Instead, values of residuals are similar for all considered time periods at frequencies below 1.25Hz.